

Supplementary information:

High-quality electrical transport using scalable CVD graphene

Sergio Pezzini,^{1,2,*} Vaidotas Mišeikis,^{1,2} Simona Pace,^{1,2} Francesco Rossella,³ Kenji Watanabe,⁴ Takashi Taniguchi,⁵ and Camilla Coletti^{1,2,*}

¹Center for Nanotechnology Innovation @NEST, Istituto Italiano di Tecnologia, Piazza San Silvestro 12, 56127 Pisa, Italy

²Graphene Labs, Istituto Italiano di Tecnologia, Via Morego 30, 16163 Genova, Italy

³NEST, Scuola Normale Superiore and Istituto Nanoscienze-CNR, Piazza San Silvestro 12, 56127 Pisa, Italy

⁴ Research Center for Functional Materials, National Institute for Materials Science, 1-1 Namiki, Tsukuba, 305-0044, Japan

⁵ International Center for Materials Nanoarchitectonics, National Institute for Materials Science, 1-1 Namiki, Tsukuba, 305-0044, Japan

E-mail: sergio.pezzini@iit.it; camilla.coletti@iit.

Raman spectroscopy of CVD-G and hBN/CVD-G/hBN

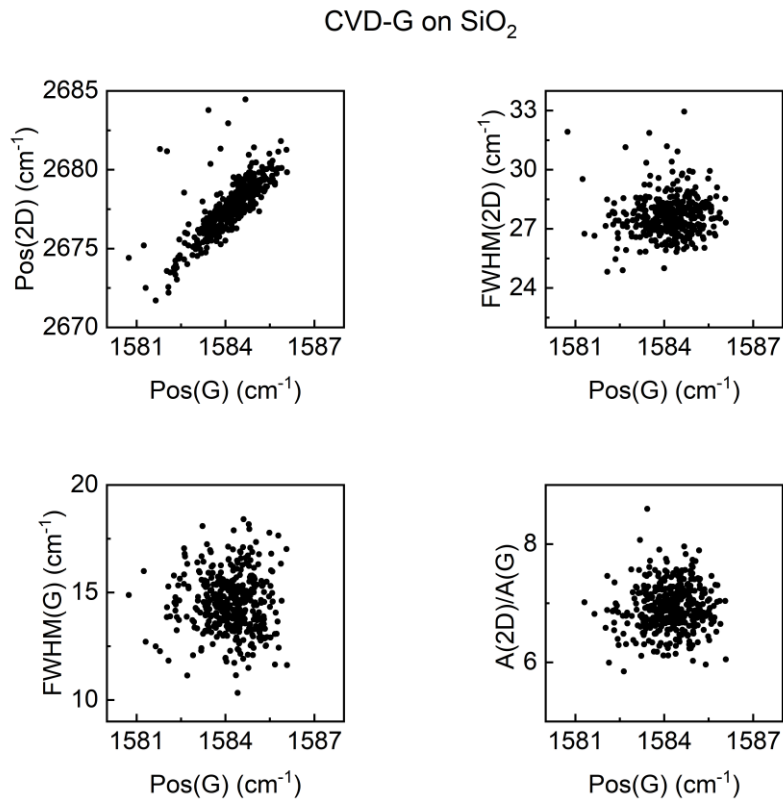


Figure S1. Raman correlation plots for CVD-G after transfer to SiO₂/Si.

In Figure S1 we show four plots correlating the main Raman parameters, measured on a CVD-G crystal from the same growth batch of the ones used for the devices discussed in the main text, after transfer to SiO₂/Si (200×200 μm² area). Pos(G) averages at 1584.2 cm⁻¹, indicating minimal uniaxial (biaxial) strain ~0.05% (0.02 %), calculated considering the influence of the finite doping level (see below) [S1]. The average FWHM(2D) is 27.7 cm⁻¹ and can be ascribed to strain fluctuations induced by the rough SiO₂ substrate within the size of the laser spot [27]. The combined average FWHM(G) = 14.5 cm⁻¹ and A(2D)/A(G) = 6.9 indicate hole doping ~100-150 meV [S2].

hBN/CVD-G/hBN

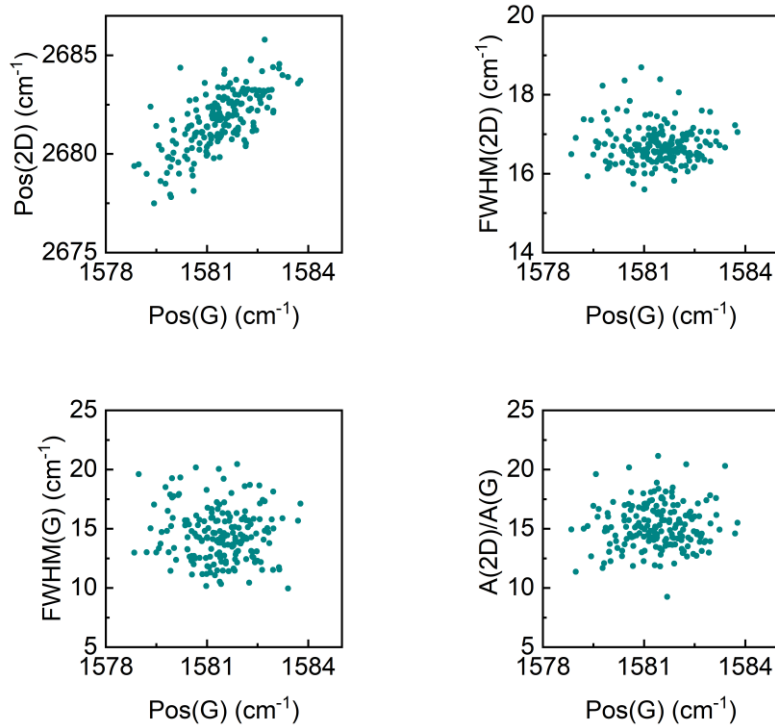


Figure S2. Raman correlation plots on a blister-free flat area of hBN/CVD-G/hBN (black dashed rectangle in main text Figure 1d). Device D1 is fabricated over this region.

The same kind of data for a bubble-free area of hBN/CVD-G/hBN (black dashed rectangle in main text Figure 1d) are shown in Figure S2. The average Pos(G) = 1581.4 cm⁻¹ is characteristic of pristine single-layer graphene [S3], while the slight blue-shift in Pos(2D) = 2681.7 cm⁻¹ can result from dielectric screening by hBN [S4]. The average FWHM(2D) = 16.7 cm⁻¹ indicates minimal strain fluctuations [27]. The average A(2D)/A(G) = 15.3 suggests a reduction of the carrier concentration to the undoped intrinsic limit [S2], which is corroborated by the field-effect electrical transport measurements (main text Figure 2).

Atomic Force Microscopy of hBN/CVD-G/hBN devices

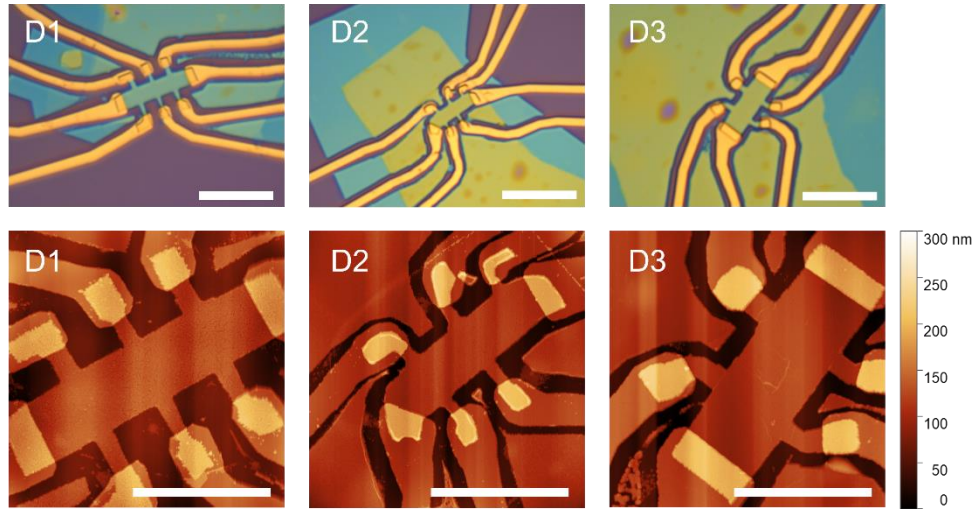


Figure S3. Upper panels: optical microscopy images of Hall bars D1-3 (scale bars are 10 μm). Lower panels: AFM images of the same devices (scale bars are 5 μm). The total thickness of the heterostructures is 70-80 nm (30-40 nm for each hBN flake). The geometrical factor for the contacts used in the resistivity measurements is $W/L = 1$ for the three samples. D1 shows larger surface roughness with respect to D2-3, due to polymer residuals after the etching step.

Gate-dependent Hall effect and estimate of the gate capacitance

To determine the back-gate capacitance per unit area (C_{bg}) of the devices, we perform Hall effect measurements as a function of the back-gate voltage in presence of $|B| = 0.5$ T, oriented perpendicular to the sample plane. We measure $R_{xy}(V_{bg})$ for positive and negative field orientation, and antisymmetrize the data according to $R_{xy} = (R_{xy}(+B) - R_{xy}(-B))/2$, to eliminate longitudinal components due to slight contact misalignment, obtaining curves as the one shown in Figure S4, left panel. Since the carrier concentration is given by $n = B/e \times 1/R_{xy} = C_{bg}(V_{bg} - V_{bg}^0)/e$, C_{bg} can be

obtained from a linear fit to $1/R_{xy}$ as a function of $(V_{bg} - V_{bg}^0)$, as shown in Figure S4, right panel. For D2, we estimate $C_{bg} = 0.97 \times 10^{-8}$ F/cm², in agreement with the calculated capacitance per unit area of two in-series parallel plate capacitors made by the SiO₂ layer (thickness $d = 300$ nm and dielectric constant $\epsilon_r = 3.7$) and the bottom hBN flake ($d = 30$ nm and $\epsilon_r = 3$).

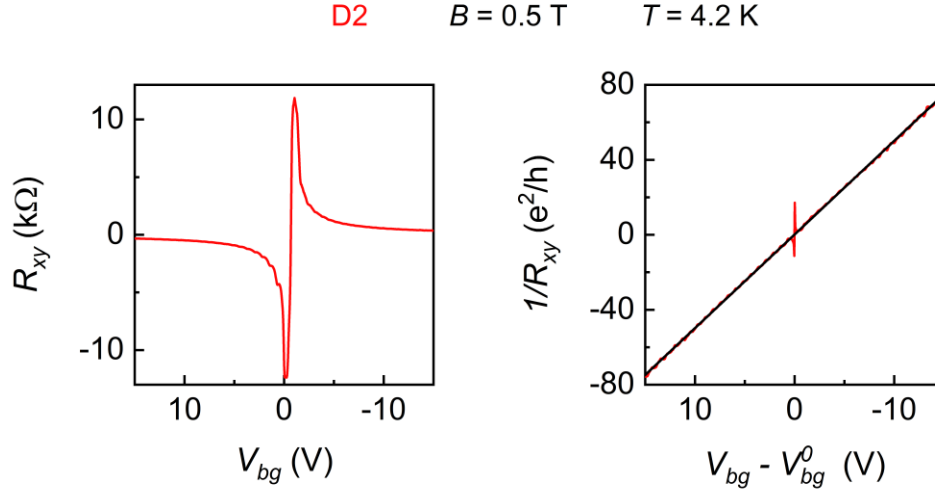


Figure S4. Left panel: field-symmetrized Hall resistance of device D2 as a function of the back-gate voltage, measured at $|B| = 0.5$ T and $T = 4.2$ K. Right panel: inverse of the Hall resistance as a function of the back-gate voltage relative to the neutrality point (red curve). The black line is a linear fit.

Room temperature conductivity for D1-2

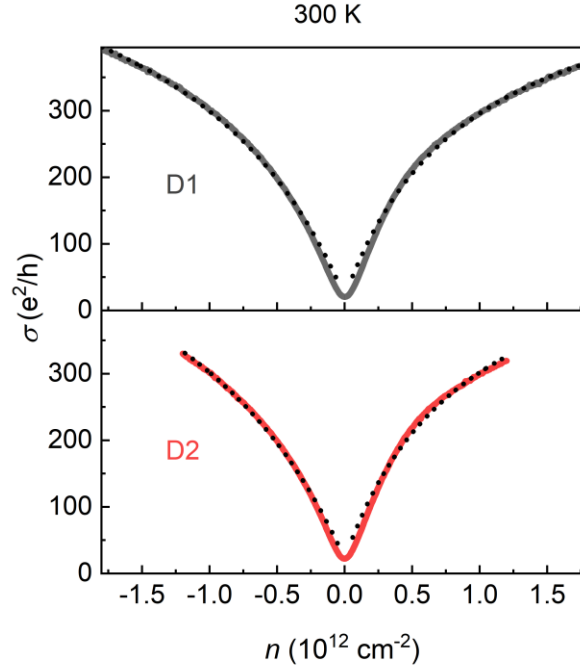


Figure S5. Room temperature conductivity as a function of carrier density for D1-2 (gray and red solid lines, respectively). The black dashed lines are fits to the data using the relation $\sigma^{-1} = (ne\mu_L + \sigma_0)^{-1} + \rho_s$ [7]. The fit is performed separately for holes and electrons and excludes the saturation region close to n^* . The fitting parameters μ_L and ρ_s for the two devices are within 3% of the values given in the main text.

Estimate of the Landau quantization onset

In order to extract the quantum scattering time (data in Figure 4b), we quantify B_{onset} for each oscillation of the low-field LL fan (Figure 4a). Here we use the $\nu = -6$ oscillation as an example.

We first inspect zoomed-in parts of the conductivity false-color map to estimate an onset region (see Figure S6, left). This provides us an interval of densities over which this specific oscillation starts to be observable, from -1.86 to $-2.16 \times 10^{10} \text{ cm}^{-2}$ in this case. For each density measured in such an interval, we look at the longitudinal resistance as a function of the magnetic field (Figure S6, right, top panel) and identify the oscillation minimum corresponding to the filling factor of interest (-6 in this case). To quantitatively address the onset, we consider the first derivative of the resistance (bottom panel, calculated after smoothing the resistance signal) and identify the onset field as corresponding to the maximum negative point in dR_{xx}/dB before the oscillation minimum. The onset field values are then averaged over the density interval to obtain B_{onset} , and τ_q is calculated.

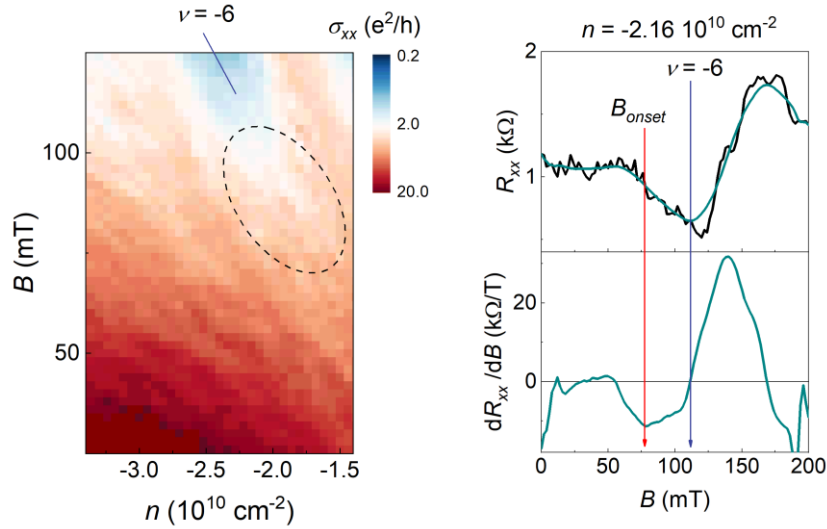


Figure S6. Left: zoom-in of main text Figure 4a, highlighting the onset of the $\nu = -6$ oscillation. Right: procedure for the determination of the onset field. Top panel: longitudinal resistance as a function of the magnetic field at density $-2.16 \times 10^{10} \text{ cm}^{-2}$. The black (dark cyan) line are experimental data (smoothed curve by adjacent averaging). Lower panel: first derivative of the

longitudinal resistance (calculated from the smoothed curve). The $\nu = -6$ minimum corresponds to a zero in the derivative, while the onset field is identified at the largest negative value of dR_{xx}/dB preceding the minimum.

Imperfect quantization in the FQH regime

As reported in the main text, we do not measure a precisely quantized value of σ_{xy} in correspondence of $\nu = -1/3$. Since field-symmetrized data at ± 12 T do not provide a substantial improvement, we exclude contacts' misalignment as the origin of this discrepancy. More likely, the lack of quantization is due to two factors related to the simple Hall bar geometry. The first one is the roughness of the etch-defined edges, which, despite common knowledge on topologically-protected phases, can strongly influence the edge states' transport: edge-free geometry [36, S5] or electrostatically-defined channels [S6] can mitigate this issue. Additionally, and possibly more importantly, perfect equilibration of the edge states at the metallic leads is required in order to observe quantization of σ_{xy} . Optimal equilibration is difficult to achieve in devices such ours, where a single global back-gate controls the carrier density both in the channel and in the contact regions. Maher *et al.* [S7] showed that a local bottom gate geometry allows tuning the sample to low filling factors, while keeping highly doped and efficient contacts via the Si back-gate. This strategy results in precise quantization in the fractional quantum Hall regime, absent otherwise. Implementing these advancements in the device fabrication should facilitate a complete establishment of FQH in CVD-G, of which our current data provide preliminary evidence.

Additional References

- [S1] Lee J E, Ahn G, Shim J, Lee Y S and Ryu S 2012 Optical separation of mechanical strain from charge doping in graphene *Nat. Commun.* **3** 1024
- [S2] Basko D M, Piscanec S and Ferrari A C 2009 Electron-electron interactions and doping dependence of the two-phonon Raman intensity in graphene *Phys. Rev. B* **80** 165413
- [S3] Ferrari A C, Meyer J C, Scardaci V, Casiraghi C, Lazzeri M, Mauri F, Piscanec S, Jiang D, Novoselov K S, Roth S and Geim A K 2006 Raman Spectrum of Graphene and Graphene Layers *Phys. Rev. Lett.* **97** 187401
- [S4] Forster F, Molina-Sanchez A, Engels S, Epping A, Watanabe K, Taniguchi T, Wirtz L and Stampfer C, 2013 Dielectric screening of the Kohn anomaly of graphene on hexagonal boron nitride *Phys. Rev. B* **88** 085419
- [S5] Polshyn H, Zhou H, Spanton E M, Taniguchi T, Watanabe K and Young A F 2018 Quantitative transport measurements of fractional quantum Hall energy gaps in edgeless graphene devices *Phys. Rev. Lett.* **121** 226801
- [S6] Ribeiro-Palau R, Chen S, Zeng Y, Watanabe K, Taniguchi T, Hone J and Dean C R 2019 High-Quality Electrostatically Defined Hall Bars in Monolayer Graphene *Nano Lett.* **19** 2583
- [S7] Maher P, Wang L, Gao Y, Forsythe C, Taniguchi T, Watanabe K, Abanin D, Papić Z, Cadden-Zimansky P, Hone J, Kim P and Dean C R 2014 Tunable fractional quantum Hall phases in bilayer graphene *Science* **345** 61